ACS OMEGA

http://pubs.acs.org/journal/acsodf

Article

# Nb-Doped $TiO_2$ with Outstanding Na/Mg-Ion Battery Performance

Hongwei Bi, Shengli Zhu,* Yanqin Liang, Hui Jiang, Zhaoyang Li, Shuilin Wu, Hao Wei, Chuntao Chang,* Hao Wang,* and Zhenduo Cui*

Cite This: *ACS Omega* 2023, 8, 5893−5900

Read Online

ACCESS | Metrics & More | Article Recommendations | Supporting Information

**ABSTRACT:** The group "beyond Li-ion" batteries (Na/Mg-ion batteries) have the advantages of abundant reserves and high theoretical specific capacity. However, the sluggish kinetics resulting from large ion radius ($Na^+$) and polarity ($Mg^{2+}$) seriously limit the battery performance. Herein, we prepared Nb-doped anatase $TiO_2$ with Ti vacancies (Nb-$TiO_2$) through a simple solvothermal and subsequent calcination process. The Nb doping widens the channels for metal ion diffusion, and the cationic vacancies can act as ion storage sites and improve the electrode conductivity. Thus, Nb-$TiO_2$ exhibits improved performance for rechargeable Na/Mg-ion batteries.

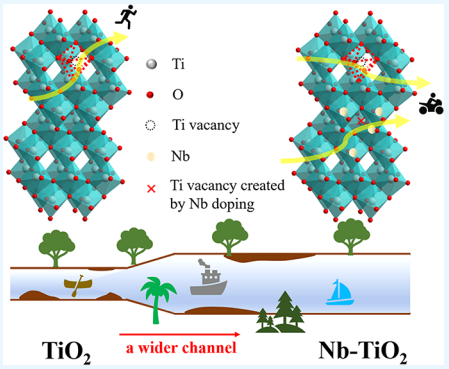


## 1. INTRODUCTION

Li-ion batteries are the most common energy storage devices that are widely used in many fields, such as electric vehicles and portable devices.[1] Nevertheless, the natural distribution and abundance of lithium cannot meet the growing demands on energy storage. Na- and Mg-ion batteries are considered appropriate candidates for substituting Li-ion batteries because of their abundant resources and high theoretical capacity. However, the sluggish diffusion kinetics of Na and Mg ions due to their strong electrostatic forces and large ion radius are serious problems, and the exploration of appropriate electrode materials for Na- and Mg-ion batteries is still a challenge.[2−6]

P,[7] Bi,[8] and $Co_3O_4$[9] electrodes based on alloying or conversion mechanisms possess a high capacity. However, the inevitable large volume expansion during the electrochemical process leads to rapid capacity fading. Insertion-type materials, such as $TiO_2$ and $Nb_2O_5$, are often used in metal-ion batteries because of their high structural stability, nontoxicity, and low cost.[10−12] These materials are usually not accompanied by various reactions during the electrochemical process. Thus, they do not have exaggerated volume change, and the simple intercalation reaction gives them good cycling stability. However, their low intrinsic electronic conductivity results in insufficient reversible capacity.[13] A method to improve the capacity and cycling performance is morphology control, which would contribute to the penetration of electrolytes.[14,15] Another effective way is to improve the electronic conductivity of $TiO_2$ through combining $TiO_2$ with carbon materials[16] or introducing defects by doping aliovalent ions such as Mo,[17] S,[18] and B[19] and annealing in various atmospheres.[20] According to previous papers,[21−23] cation vacancies play a crucial role in battery energy storage. The presence of cation vacancies can decrease the energy barrier for ion intercalation, increase the electronic conductivity, and promote the charge transfer process. More importantly, cation vacancies can act as additional energy storage sites due to their negative charge character.[24] A previous paper also proved that undoped $TiO_2$ with Ti vacancies exhibited better battery performance than stoichiometric $TiO_2$.[25] However, further improvement is necessary for industrial applications. Tuning lattice structures through doping is a kind of appropriate approach. Some works reported that doping metal elements with higher valence than $Ti^{4+}$ (such as $W^{6+}$ and $Nb^{5+}$) in $TiO_2$ would introduce Ti vacancies and thus improve the electronic conductivity.[26,27] In addition, the large radius of doping metals, such as $Mo^{5+}$ and $Nb^{5+}$, would widen the ion diffusion channel and promote ion diffusion kinetics.

The present work prepared Nb-doped $TiO_2$ with abundant Ti vacancies. The $Nb^{5+}$ in $TiO_2$ can widen the diffusion channels and introduce cation vacancies. Moreover, the Nb-doped $TiO_2$ exhibits a higher capacity and better cycling performance in Na/Mg-ion batteries than the undoped $TiO_2$.

## 2. EXPERIMENTAL SECTION

**2.1. Synthesis of Nb-$TiO_2$ with Ti Vacancies.** The Nb-doped $TiO_2$ was prepared according to a previous study.[28] In

Received: December 1, 2022
Accepted: January 20, 2023
Published: January 30, 2023

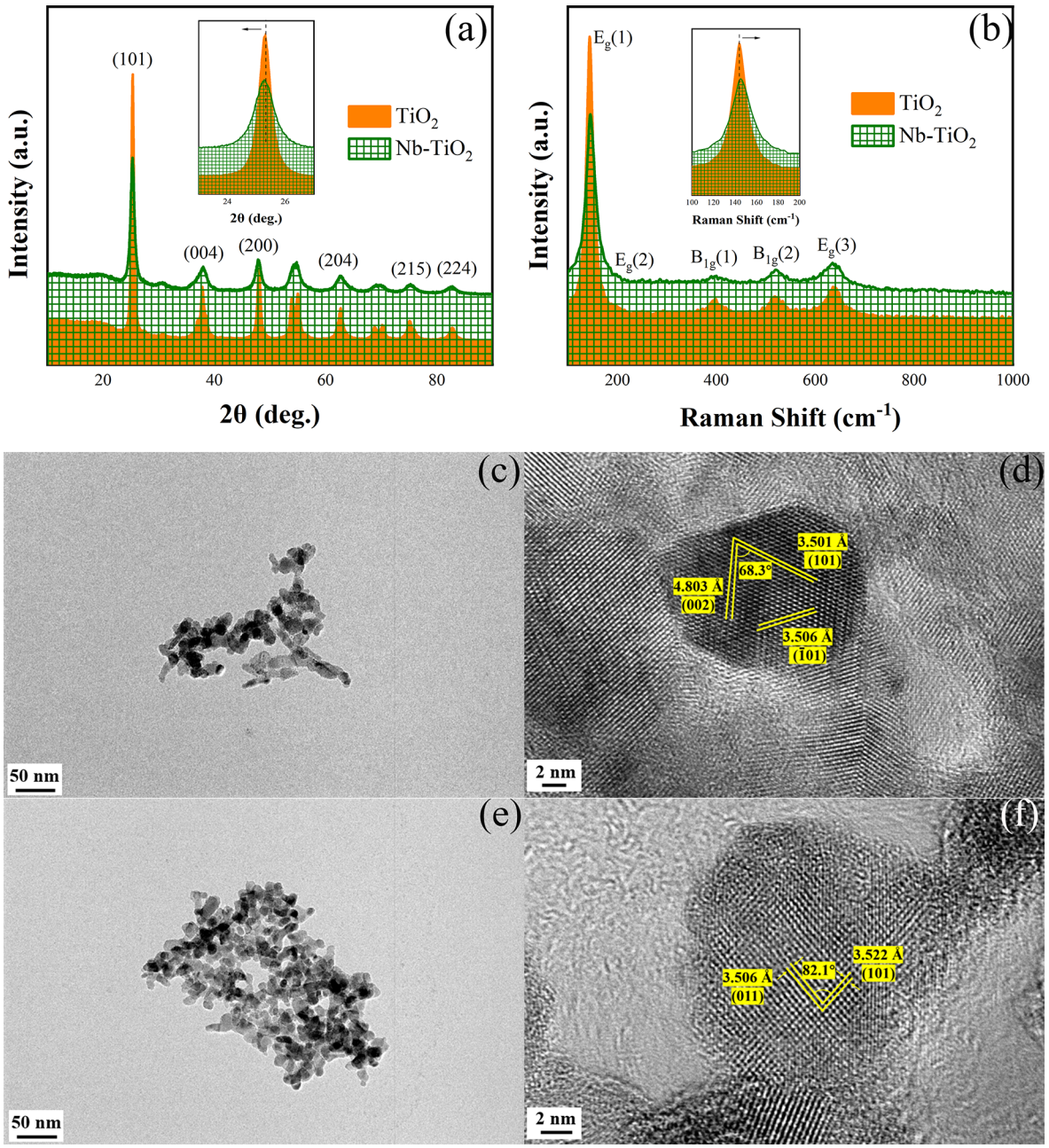


**Figure 1.** (a) XRD patterns and enlarged XRD patterns for $TiO_2$ and Nb-$TiO_2$. (b) Raman spectra and enlarged Raman spectra of $TiO_2$ and Nb-$TiO_2$ after calcination. TEM images of (c) $TiO_2$ and (e) Nb-$TiO_2$. HRTEM images of (d) $TiO_2$ and (f) Nb-$TiO_2$.

detail, 1 mL of TBT was added into a mixed solution of 10 mL of glycerol and 30 mL of ethanol under magnetic stirring, and 44 $\mu$L of niobium(V) ethoxide was added to the solution. After stirring for 30 min, the mixed solution was transferred into a 100 mL Teflon-lined autoclave and heated at 180 °C for 24 h. The powders were washed with absolute ethanol five times and dried at 60 °C for 12 h. Finally, the powders were calcined in air at 470 °C for 1 h with a heating rate of 5 °C/min (denoted as Nb-$TiO_2$). Undoped $TiO_2$ powders were also synthesized with the same procedure without niobium(V) ethoxide addition during the solvothermal process.

**2.2. Material Characterizations.** The phase composition was determined by X-ray diffraction (XRD, HaoYuan DX-2700BH) and Raman spectroscopy (Raman, Thermo Scientific DXR Spectrometer). Morphological characteristics and chemical distribution were examined using a transmission electron microscope (TEM, JEOL-2100) equipped with an energy-dispersive X-ray spectroscope (EDX). The surface chemical state was tested using an X-ray photoelectron spectroscope (XPS, Axis Supra) with Al K$\alpha$ radiation. All the binding energies were calibrated using the C 1s peak as a standard. Electron paramagnetic resonance (EPR, JES-FA200 spectrometer) was used to test Ti vacancies.

**2.3. Electrochemical Characterizations.** Working electrode slurries were prepared by mixing active materials ($TiO_2$/Nb-$TiO_2$), polyvinylidene fluoride (PVDF), and Super P with a weight ratio of 70:15:15, and 800 $\mu$L of *N*-methyl-2-pyrrolidone (NMP) was used as the solvent. After stirring for 12 h, the slurries were cast on Cu/stainless steel foils and dried at 120 °C for 12 h in a vacuum oven.



https://doi.org/10.1021/acsomega.2c07689
ACS Omega 2023, 8, 5893−5900

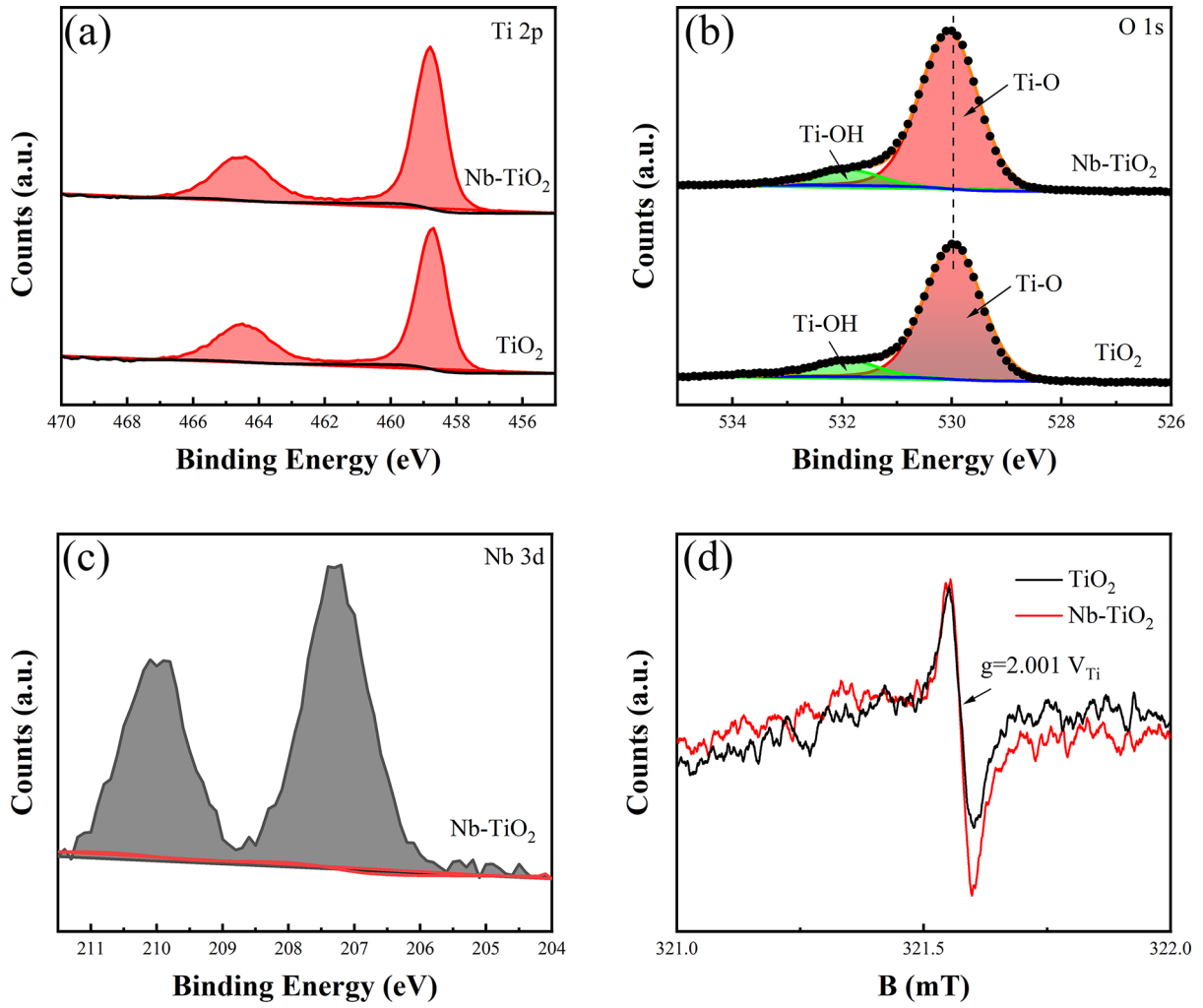


**Figure 2.** High-resolution XPS spectra of (a) Ti 2p, (b) O 1s, and (c) Nb 3d of $TiO_2$ and Nb-$TiO_2$. (d) EPR data analysis of $TiO_2$ and Nb-$TiO_2$ at room temperature.

Thin Mg slice/Na foil served as counter electrodes. Glass fiber filter (GF/C, Whatman) was used as the separator, and the electrolyte was 0.4 M $(MgPhCl)_2$ (pheylmagnesium chloride)-$AlCl_3$ in THF (tetrahydrofuran) = 100 vol %, following a previously reported procedure[29] (1.0 M $NaPF_6$ in EC (ethylene carbonate):DMC (dimethyl carbonate) = 1:1(vol %) with 5% FEC (fluoroethylene carbonate) added for Na-ion batteries). A LAND CT2001A multichannel battery test system was used to conduct the galvanostatic charge/discharge (GCD) experiments at room temperature (the test voltage range: 0.01 and 2.0 V vs $Mg^{2+}$/Mg for Mg-ion batteries and 0.01 and 3.0 V vs $Na^+$/Na for Na-ion batteries). The specific capacity was calculated based on the active material's loading mass, and each electrode's mass loading was about 0.8−1.2 mg/$cm^2$. Cyclic voltammetry (CV) measurements were conducted using an electrochemistry workstation (Gamry Interface 1000) at scanning rates of 0.2, 0.5, 1.0, and 2.0 mV $s^{-1}$. Galvanostatic intermittent titration technique (GITT) measurements were conducted on the LAND CT2001A system during the 10th discharge process, and the cells were intermittently discharged at 50 mA $g^{-1}$ for 5 min followed by 20 min of relaxation. Electrochemical impedance spectroscopy (EIS) was performed using the same electrochemistry workstation. The AC amplitude was 10 mV, and the frequency range was 100 kHz to 0.01 Hz.

## 3. RESULTS AND DISCUSSION

Figure S1a shows the XRD patterns of $TiO_2$ and Nb-$TiO_2$ before calcination. The two samples show similar XRD patterns, indicating that the Nb addition would not affect the structure of the precursor. A published article assigned this unknown substance to titanium glycerolate (TiGly).[28] After calcination at 470 °C for 1 h, TiGly transforms to anatase $TiO_2$, as shown in Figure 1a. The precursor of $TiO_2$ is parallel chains containing Ti and organic ligands. The calcination process will remove organic groups, and the remaining Ti-O-Ti will be tied together to form $TiO_2$ crystals. During the calcination process, the existence of organic groups results in an O-rich environment locally around Ti atoms, which would favor the formation of Ti vacancies. Compared with $TiO_2$, the (101) peak of Nb-$TiO_2$ shifts to a lower angle, indicating a larger interplanar spacing. This is due to the larger ion radius of $Nb^{5+}$ (0.64 Å), causing a slight change in $TiO_2$ crystalline.[30] The Raman spectra in Figure 1b also verify the successful synthesis of Nb-doped anatase $TiO_2$. Both $TiO_2$ and Nb-$TiO_2$ show the characteristic peaks of anatase, which center at 143, 196, 397, 517, and 639 $cm^{-1}$. Compared with $TiO_2$, peaks for Nb-$TiO_2$ broaden, which could be attributed to more serious non-stoichiometry due to more Ti vacancies in Nb-$TiO_2$.[31] In addition, after incorporating Nb into $TiO_2$, the main peak


https://doi.org/10.1021/acsomega.2c07689
ACS Omega 2023, 8, 5893−5900

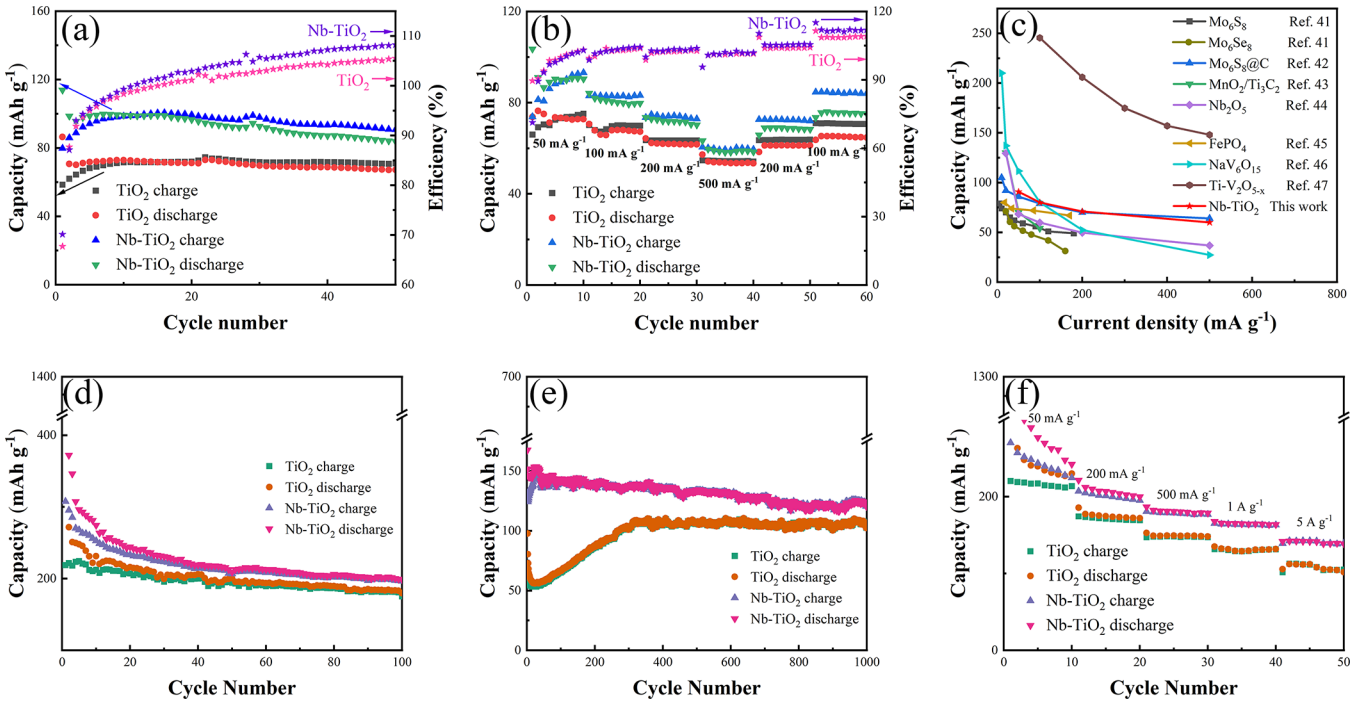


**Figure 3.** Electrochemical properties of samples assembled as Mg-ion batteries: (a) cycling performance of $TiO_2$ and Nb-$TiO_2$ at 100 mA $g^{-1}$ for 50 cycles; (b) rate performance of $TiO_2$ and Nb-$TiO_2$ at currents of 50, 100, 200, and 500 mA $g^{-1}$; and (c) comparison of rate performance between Nb-$TiO_2$ and published cathode materials for Mg-ion batteries. Electrochemical properties of samples assembled as Na-ion batteries: (d) cycling performance of $TiO_2$ and Nb-$TiO_2$ at 50 mA $g^{-1}$ for 100 cycles; (e) cycling performance of $TiO_2$ and Nb-$TiO_2$ at 1000 mA $g^{-1}$ for 1000 cycles; and (f) rate performance of $TiO_2$ and Nb-$TiO_2$ at currents of 50, 200, 500, 1000, and 5000 mA $g^{-1}$.

centered at 143 $cm^{-1}$ has a blue shift. The change in Raman vibration mode could be related to the following factors: (1) large $Nb^{5+}$ dopants cause the $TiO_2$ lattice expansion,[32] and (2) the presence of more Ti vacancies induces more disorder of $TiO_2$ crystalline.[33]

Figure 1c–f shows the TEM images of $TiO_2$ and Nb-$TiO_2$. The two samples both appear as nanoparticles without a noticeable difference. As shown in Figure 1d, two interplanar spacings of 3.501 and 4.803 Å with an angle of 68.3° can be indexed as the (101) and (002) facets of anatase $TiO_2$, respectively. Meanwhile, the spacings of 3.506 and 3.522 Å with an angle of 82.1° correspond to the facets of (011) and (101) of Nb-$TiO_2$ (Figure 1f). The gradual expansion of lattice spacing (such as the (101) facet) in Nb-$TiO_2$ is also owing to the relatively larger radius of $Nb^{5+}$, which is consistent with the XRD results. Furthermore, the corresponding EDX mapping for Nb-$TiO_2$ shows the uniform element distribution of Ti, O, and Nb (Figure S3).

The chemical states of Ti, O, and Nb are further verified by XPS analysis (Figure 2). Figure 2a shows the high-resolution XPS spectra of Ti 2p. The Ti $2p_{1/2}$ and Ti $2p_{3/2}$ peaks of $TiO_2$ are located at 464.4 and 458.7 eV, respectively. Meanwhile, the two peaks of Nb-doped $TiO_2$ slightly shift to higher binding energies with a gap of 5.7 eV, indicating the absence of $Ti^{3+}$ in Nb-$TiO_2$.[34] The spectra of O 1s can be divided into two peaks centered at 530 and 532 eV, which correspond to lattice oxygen (Ti-O) and Ti-OH, respectively.[35,36] The binding energy of lattice oxygen in O 1s of Nb-doped $TiO_2$ shifts to a higher binding energy than $TiO_2$. Moreover, the changes in binding energy for Ti 2p and the lattice O are mainly due to the $Nb^{5+}$ having a greater electronegativity (1.6) than the $Ti^{4+}$(1.54); more electrons would be attracted by $Nb^{5+}$. In addition, the Nb $3d_{3/2}$ and Nb $3d_{5/2}$ peaks appear at 210 and 207.2 eV, respectively. The spin–orbit splitting with 2.8 eV demonstrates that Nb still exists in the high valence state of 5+ rather than reduced to 4+.[27] Therefore, according to the Kröger–Vink notation,[37,38] the formation of Ti vacancies in Nb-$TiO_2$ can be expressed as eq 1:

$$\frac{1}{2}Nb_2O_5 + Ti_{Ti}^{\times} \rightarrow Nb_{Ti}^{\cdot} + \frac{1}{4}V_{Ti}^{''''} + TiO_2 + \frac{1}{4}O_2 \quad (1)$$

As Nb atoms incorporate into the $TiO_2$ crystalline structure, one Ti vacancy is created for every four titanium atoms substituted. Electron paramagnetic resonance (EPR) is an effective way to examine the existence of defects in Nb-$TiO_2$. Nb-$TiO_2$ presents the signal feedback at $g$ = 2.001 (Figure 2d), which can be assigned to Ti vacancies the EPR signals of $Ti^{3+}$ defects, $O_2^-$, and oxygen vacancies are located at $g$ = 1.960–1.990, 2.020, and 2.003, respectively.[28,39]

The electrochemical performance of $TiO_2$ and Nb-$TiO_2$ with cation vacancies are evaluated and compared using GCD experiments. Figure S4 compares the 1st, 2nd, 5th, 20th, and 50th cycle GCD curves at 100 mA $g^{-1}$ in Mg-ion batteries. Upon cycling, the sloping characteristic can be observed in both $TiO_2$ and Nb-$TiO_2$. In addition, Nb-$TiO_2$ has an initial discharge/charge capacity of 113.8/79.8 mAh $g^{-1}$ with an initial Coulombic efficiency (ICE) of 70%. The inevitable capacity loss in the process originates from the trapped $Mg^{2+}$ and electrolyte decomposition.[40] In the subsequent cycles, Nb-$TiO_2$ still possesses a specific capacity of 85 mAh $g^{-1}$, while $TiO_2$ only displays a value of 67 mAh $g^{-1}$ (Figure 3a). Similarly, Nb-$TiO_2$ possesses better rate performance than $TiO_2$. At currents of 50, 100, 200, and 500 mA $g^{-1}$, the discharge capacities of Nb-$TiO_2$ are 90, 80.7, 71, and 60 mAh $g^{-1}$, respectively. Compared with other electrode materials based on the intercalation mechanism, Nb-$TiO_2$ shows


https://doi.org/10.1021/acsomega.2c07689
ACS Omega 2023, 8, 5893–5900

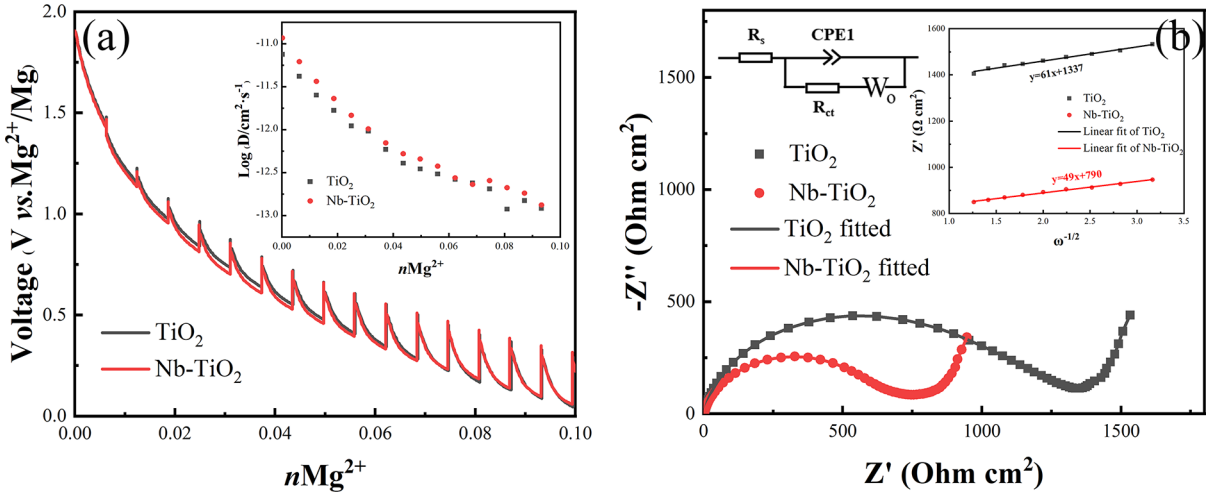


**Figure 4.** (a) GITT curves at the 10th cycle and the calculated $Mg^{2+}$ diffusion coefficient in Mg-ion batteries. (b) Nyquist plots and the corresponding equivalent circuit of $TiO_2$ and Nb-$TiO_2$ electrodes and Zreal vs $\omega^{-1/2}$ plot at a low-frequency region.

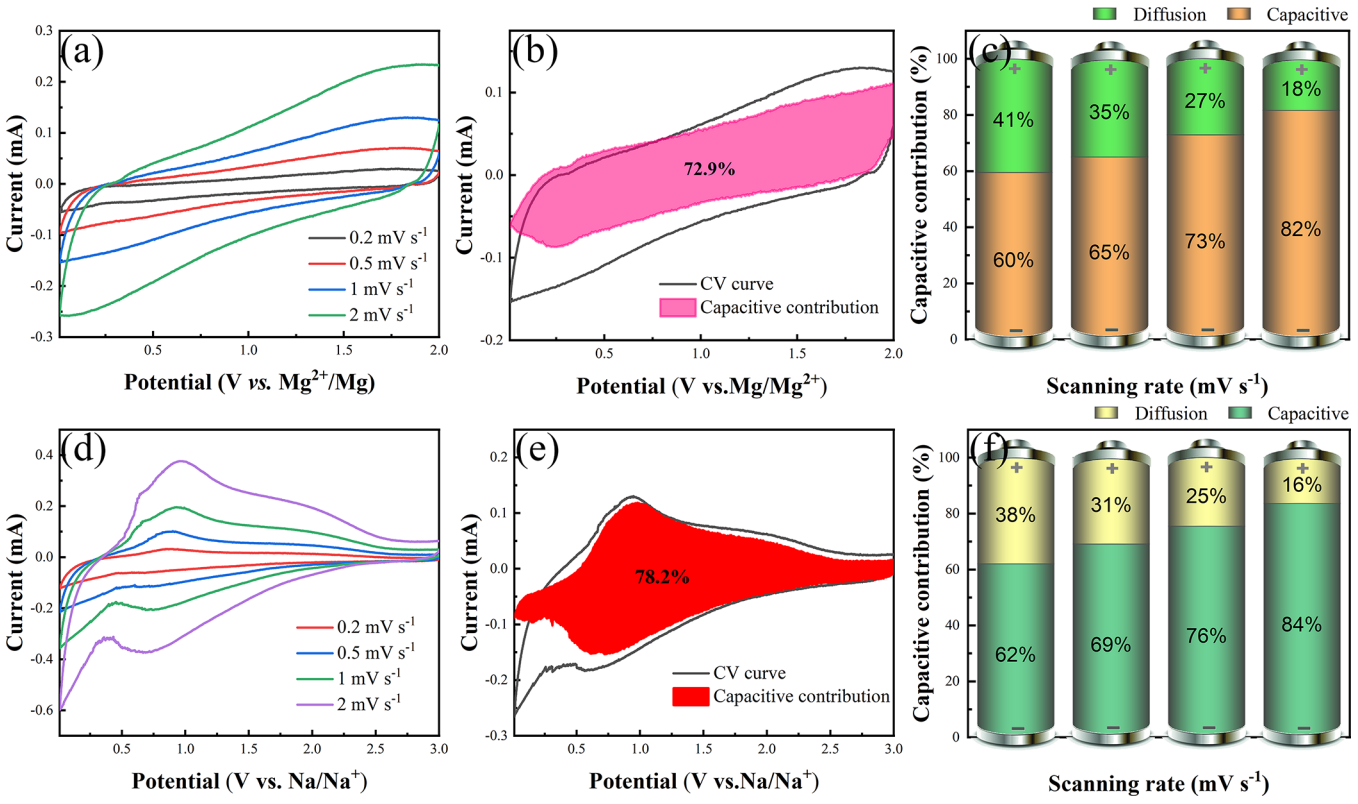


**Figure 5.** Mg-ion battery: (a) CV curves of the Nb-$TiO_2$ electrode at various scan rates (from 0.2 to 2 mV $s^{-1}$); (b) CV curve and pseudo-capacitive contribution represented by the pink shaded area at 1 mV $s^{-1}$; and (c) variation of the pseudo-capacitive contribution with increasing CV scanning rate. Na-ion battery: (d) CV curves of the Nb-$TiO_2$ electrode at various scan rates (from 0.2 to 2 mV $s^{-1}$); (e) CV curve and pseudo-capacitive contribution represented by the red shaded area at 1 mV $s^{-1}$; and (f) variation of the pseudo-capacitive contribution with increasing CV scanning rate.

competitive potential because of the excellent battery performance and simple preparation process,[41−46] although it has a large gap with the $V_2O_5$ electrode material[47] (Figure 3c). The performance of Na-ion batteries has also been improved significantly by Nb doping. Nb-doped $TiO_2$ can retain a specific capacity of 198.7 (100th cycle) and 121.7 mAh $g^{-1}$ (1000th cycle) at 50 and 1000 mA $g^{-1}$ (Figure 3d,e), respectively, which is competitive compared with the as-reported $TiO_2$-based materials, even for hybrid electrodes composed of titanium dioxide and carbon materials (Table S1 and S2). It is worth noting that the capacity of $TiO_2$ and Nb-$TiO_2$ decreases first and then increases at a high current density. Furthermore, the capacity rise process in $TiO_2$ lasts longer than Nb-$TiO_2$. According to previous papers, an electrode based on $TiO_2$ needs several cycles to activate during the charge/discharge process.[48−50] However, $TiO_2$ and Nb-$TiO_2$ in this study do not experience the same amount of time during this step because Nb doping would provide wider



https://doi.org/10.1021/acsomega.2c07689
ACS Omega 2023, 8, 5893−5900

diffusion channels for $Na^+$, and then, $Na^+$ is more likely to enter the energy storage sites of $TiO_2$ lattice. The rate performance of Na-ion batteries is evaluated by GCD testing under various currents from 50 to 5000 mA $g^{-1}$. The capacity of Nb-$TiO_2$ is always higher than that of $TiO_2$. Even at a higher current density of 5000 mA $g^{-1}$, Nb-$TiO_2$ still possesses a capacity of 138.6 mAh $g^{-1}$, nearly 27% higher than $TiO_2$.

The biggest obstacle for Na/Mg-ion batteries using $TiO_2$ is the sluggish diffusion kinetics resulting from the large ion radius ($Na^+$) or strong force between $Mg^{2+}$ and $TiO_2$ lattice. To verify the positive effect of Nb doping, GITT and EIS experiments were carried out in both Mg- and Na-ion batteries (Figure 4a). The GITT experiments were conducted during the 10th discharge process in Mg-ion batteries. The higher diffusion coefficient values of Nb-$TiO_2$ indicate a more favorable local environment for $Mg^{2+}$ diffusion. It is worth noting that with the increase in the intercalation of $Mg^{2+}$, the gap in the diffusion coefficients between $TiO_2$ and Nb-$TiO_2$ gradually becomes smaller. This is because the crystal structures of the two samples become similar when $Mg^{2+}$ gradually fills the Ti vacancies in Nb-$TiO_2$. Figure 4b presents the Nyquist plots of $TiO_2$ and Nb-$TiO_2$ after the first lap discharge (Na-ion battery), and the corresponding equivalent circuit is shown in the inset. $R_s$ represents the electrolyte resistance in the equivalent circuit, $R_{ct}$ means the charge-transfer impedance, CPE1 is the double-layer capacitance, and $W_o$ is the Warburg impedance.[51] The fitted values for $R_s$ and $R_{ct}$ are listed in Table S3. The lower $R_{ct}$ value of Nb-$TiO_2$ (661.7 Ω $cm^2$) than $TiO_2$ (1212 Ω $cm^2$) proves that adding Nb can effectively promote charge transfer ability. Moreover, the $Na^+$ diffusion coefficient of two electrodes can also be calculated according to eqs 2 and 3:[52]

$$Z' = R_s + R_{ct} + \sigma\omega^{-1/2} \tag{2}$$

$$D_{Na^+} = \frac{R^2T^2}{2n^4A^2F^4C^2\sigma^2} \tag{3}$$

where $R_s$ and $R_{ct}$ correspond to the electrolyte resistance and charge transfer resistance. $\sigma$ is the Warburg factor, and $\omega$ is the angular frequency. The value of $\sigma$ is related to the slope of the line $Z'$ vs $\omega^{-1/2}$, which is shown in Figure 4b ($TiO_2$: $\sigma$ = 61, Nb-$TiO_2$: $\sigma$ = 49). In eq 3, $R$ is the gas constant, $T$ is the absolute temperature, $n$ is the number of electrons per molecule in reaction, $F$ is the Faraday constant, and $C$ is the molar density of $Na^+$. Based on the fitted value of $\sigma$ in eq 2, $D_{Na^+}$ in Nb-$TiO_2$ is 1.54 times higher than that in $TiO_2$. Therefore, Nb doping can significantly accelerate the diffusion of metal ions during the electrochemical process.

Both diffusion and pseudo-capacitance can influence the total capacity of metal-ion batteries. The storage mechanism was investigated using CV tests at different scan rates of 0.2, 0.5, 1 and 2 mV $s^{-1}$ in Mg- and Na-ion batteries (as shown in Figure 5a,d). The rectangle shape curves of Nb-$TiO_2$ in Mg-ion batteries show that diffusion and pseudo-capacitance contribute to the total capacity.[40] The capacitive contribution can be quantified based on eq 4[34]

$$i(V) = k_1v + k_2v^{1/2} \tag{4}$$

where $i(V)$ is the current related to the scan rates and $k_1v$ and $k_2v^{1/2}$ represent the percentage of capacitive contribution and diffusion-controlled intercalation, respectively. For instance, the capacitive process in the Mg-ion battery can contribute 72.9% of the total capacity at a scan rate of 1 mV $s^{-1}$ (Figure 5b). The contribution ratio of the pseudo-capacitive-controlled process for the Nb-$TiO_2$ electrode increases with increasing sweep rate, indicating that the capacitance-controlled processes would dominate the entire electrochemical process at a high sweep rate. In addition, the contribution of pseudo-capacitive in Na-ion batteries using Nb-$TiO_2$ displays the same trend as that in Mg-ion batteries. Therefore, from the above structural characterizations and electrochemical analyses, Nb doping significantly affects the $TiO_2$ crystalline structure and thus leads to improved battery performance. These beneficial effects can be summarized in the following aspects: (a) When Nb substitutes Ti in the $TiO_2$ crystalline structure, the charge compensation effect leads to Ti vacancies, which would serve as additional storage sites for metal ions. (b) The diffusion pathway is broadened due to the introduction of a larger ion radius of $Nb^{5+}$. (c) Missing part Ti atoms in the $TiO_2$ lattice accelerates the charge transfer kinetics. The mechanism of Nb doping to improve electrode performance is shown in Figure 6.

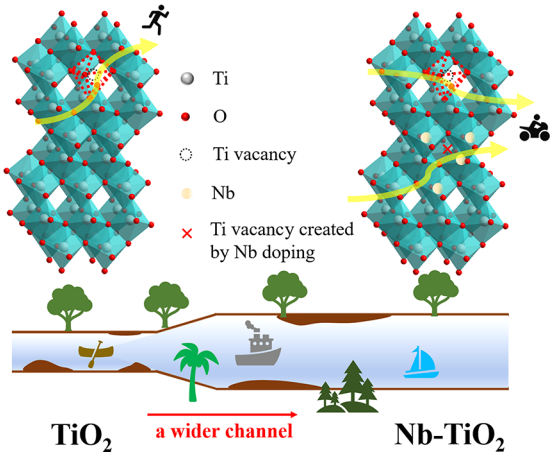


**Figure 6.** Schematic diagram of insertion of $Na^+$ into Nb-$TiO_2$.

## 4. CONCLUSIONS

In summary, the Nb-doped $TiO_2$ electrode material was synthesized by a simple solvothermal and subsequent calcination process. The Nb doping broadens the ion diffusion channels and generates more Ti cation vacancies. The cation vacancies provide more ion storage sites. The missing part of Ti atoms in the $TiO_2$ lattice accelerates the charge transfer kinetics. Nb-$TiO_2$ exhibits high capacity and good cycling ability for the Mg- and Na-ion batteries. In Mg-ion batteries, Nb-$TiO_2$ possesses a specific capacity of 85 mAh $g^{-1}$ (50th cycle at 100 mA $g^{-1}$), while $TiO_2$ only displays a value of 67 mAh $g^{-1}$. In the Na-ion battery, at 1 A $g^{-1}$, the capacity of Nb-$TiO_2$ is nearly 27% higher than $TiO_2$. The simple preparation process and outstanding battery performance make Nb-$TiO_2$ competitive.

## ■ ASSOCIATED CONTENT

### Supporting Information

The Supporting Information is available free of charge at https://pubs.acs.org/doi/10.1021/acsomega.2c07689.

Additional XRD, Raman spectra, EDX, charge−discharge curves, CV results, specific capacities, properties, and electrochemical performance comparison with



https://doi.org/10.1021/acsomega.2c07689
ACS Omega 2023, 8, 5893−5900

those from published articles, and fitted values for EIS data (PDF)

## AUTHOR INFORMATION


### Corresponding Authors

**Shengli Zhu** − *School of Materials Science and Engineering, Tianjin University, Tianjin 300350, China; Tianjin Key Laboratory of Composite and Functional Materials, Tianjin 300350, China;* orcid.org/0000-0002-0190-2626; Email: slzhu@tju.edu.cn

**Chuntao Chang** − *School of Mechanical Engineering, Dongguan University of Technology, Dongguan 523808, China*; Email: changct@dgut.edu.cn

**Hao Wang** − *Institute for Material Research, Tohoku University, Sendai 9808577, Japan*; Email: hao.wang.e4@tohoku.ac.jp

**Zhenduo Cui** − *School of Materials Science and Engineering, Tianjin University, Tianjin 300350, China; Tianjin Key Laboratory of Composite and Functional Materials, Tianjin 300350, China*; Email: zdcui@tju.edu.cn

### Authors

**Hongwei Bi** − *School of Materials Science and Engineering, Tianjin University, Tianjin 300350, China*

**Yanqin Liang** − *School of Materials Science and Engineering, Tianjin University, Tianjin 300350, China; Tianjin Key Laboratory of Composite and Functional Materials, Tianjin 300350, China;* orcid.org/0000-0001-6317-8314

**Hui Jiang** − *School of Materials Science and Engineering, Tianjin University, Tianjin 300350, China; Tianjin Key Laboratory of Composite and Functional Materials, Tianjin 300350, China;* orcid.org/0000-0002-4577-2886

**Zhaoyang Li** − *School of Materials Science and Engineering, Tianjin University, Tianjin 300350, China; Tianjin Key Laboratory of Composite and Functional Materials, Tianjin 300350, China*

**Shuilin Wu** − *School of Materials Science and Engineering, Tianjin University, Tianjin 300350, China; Tianjin Key Laboratory of Composite and Functional Materials, Tianjin 300350, China*

**Hao Wei** − *Cell Development Department, BYD Company Limited, Shenzhen 518116, China*

Complete contact information is available at: https://pubs.acs.org/10.1021/acsomega.2c07689


### Author Contributions

H.B. and S.Z. conceived the project. H.B., Y.L., J.H., Z.L., S.W., and H.W. proposed the strategy for experimental design and analyzed the data. H.B. wrote the draft, and S.Z., H.W., and Z.C. revised the manuscript. All authors have given approval to the final version of the article.

### Notes

The authors declare no competing financial interest.

## ACKNOWLEDGMENTS

The authors appreciate the support from the Natural Science Foundation of China (No. 52271152).

## REFERENCES


(1) Xu, X.; Chen, B.; Hu, J.; Sun, B.; Liang, X.; Li, N.; Yang, S. A.; Zhang, H.; Huang, W.; Yu, T. Heterostructured $TiO_2$ spheres with tunable interiors and shells toward improved packing density and pseudocapacitive sodium storage. *Adv. Mater.* **2019**, *31*, 1904589.

(2) Gan, Q.; He, H.; Zhu, Y.; Wang, Z.; Qin, N.; Gu, S.; Li, Z.; Luo, W.; Lu, Z. Defect-assisted selective surface phosphorus doping to enhance rate capability of titanium dioxide for sodium ion batteries. *ACS Nano* **2019**, *13*, 9247−9258.

(3) Xiao, L.; Ji, F.; Zhang, J.; Chen, X.; Fang, Y. Doping regulation in polyanionic compounds for advanced sodium-ion batteries. *Small* **2023**, 2205732.

(4) Huang, Z.-X.; Zhang, X.-L.; Zhao, X.-X.; Heng, Y.-L.; Wang, T.; Geng, H.; Wu, X.-L. Hollow $Na_{0.62}K_{0.05}Mn_{0.7}Ni_{0.2}Co_{0.1}O_2$ polyhedra with exposed stable {001} facets and K riveting for sodium-ion batteries. *Sci. China Mater.* **2023**, 1.

(5) Yi, T.-F.; Pan, J.-J.; Wei, T.-T.; Li, Y.; Cao, G. NiCo2S4-based nanocomposites for energy storage in supercapacitors and batteries. *Nano Today* **2020**, *33*, No. 100894.

(6) Wang, M.-Y.; Zhao, X.-X.; Guo, J.-Z.; Nie, X.-J.; Gu, Z.-Y.; Yang, X.; Wu, X.-L. Enhanced electrode kinetics and properties via anionic regulation in polyanionic $Na_{3+x}V_2(PO_4)_{3-x}(P_2O_7)_x$ cathode material. *Green Energy Environ.* **2022**, *7*, 763−771.

(7) Zhu, Y.; Wen, Y.; Fan, X.; Gao, T.; Han, F.; Luo, C.; Liou, S.; Wang, C. Red phosphorus-single-walled carbon nanotube composite as a superior anode for sodium ion batteries. *ACS Nano* **2015**, *9*, 3254−3264.

(8) Wu, H.; Cui, Y. Designing nanostructured Si anodes for high energy lithium ion batteries. *Nano Today* **2012**, *7*, 414−429.

(9) Chen, D.; Peng, L.; Yuan, Y.; Zhu, Y.; Fang, Z.; Yan, C.; Chen, G.; Shahbazian-Yassar, R.; Lu, J.; Amine, K.; Yu, G. Two-dimensional holey $Co_3O_4$ nanosheets for high-rate alkali-ion batteries: From rational synthesis to in situ probing. *Nano Lett.* **2017**, *17*, 3907−3913.

(10) Ni, J.; Fu, S.; Wu, C.; Maier, J.; Yu, Y.; Li, L. Self-supported nanotube arrays of sulfur-doped $TiO_2$ enabling ultrastable and robust sodium storage. *Adv. Mater.* **2016**, *28*, 2259−2265.

(11) Yi, T.-F.; Wei, T.-T.; Li, Y.; He, Y.-B.; Wang, Z.-B. Efforts on enhancing the Li-ion diffusion coefficient and electronic conductivity of titanate-based anode materials for advanced Li-ion batteries. *Energy Storage Mater.* **2020**, *26*, 165−197.

(12) Yi, T.-F.; Sari, H. M. K.; Li, X.; Wang, F.; Zhu, Y.-R.; Hu, J.; Zhang, J.; Li, X. A review of niobium oxides based nanocomposites for lithium-ion batteries, sodium-ion batteries and supercapacitors. *Nano Energy* **2021**, *85*, No. 105955.

(13) Lou, S.; Zhao, Y.; Wang, J.; Yin, G.; Du, C.; Sun, X. Ti-based oxide anode materials for advanced electrochemical energy storage: lithium/sodium ion batteries and hybrid pseudocapacitors. *Small* **2019**, *15*, 1904740.

(14) Yang, X.; Wang, C.; Yang, Y.; Zhang, Y.; Jia, X.; Chen, J.; Ji, X. Anatase $TiO_2$ nanocubes for fast and durable sodium ion battery anodes. *J. Mater. Chem. A* **2015**, *3*, 8800−8807.

(15) Kim, K. T.; Ali, G.; Chung, K. Y.; Yoon, C. S.; Yashiro, H.; Sun, Y. K.; Lu, J.; Amine, K.; Myung, S. T. Anatase titania nanorods as an intercalation anode material for rechargeable sodium batteries. *Nano Lett.* **2014**, *14*, 416−422.

(16) Luo, H.; Chen, Y.; Huang, J.; Chen, Z.; Xia, X.; Li, J.; Liu, H. 3.3 nm-sized $TiO_2$/carbon hybrid spheres endowed with pseudocapacitance-dominated superhigh-rate Li-ion and Na-ion storage. *Nanoscale* **2020**, *12*, 7366−7375.

(17) Liao, H.; Xie, L.; Zhang, Y.; Qiu, X.; Li, S.; Huang, Z.; Hou, H.; Ji, X. Mo-doped gray anatase $TiO_2$ : lattice expansion for enhanced sodium storage. *Electrochim. Acta* **2016**, *219*, 227−234.

(18) He, H.; Huang, D.; Pang, W.; Sun, D.; Wang, Q.; Tang, Y.; Ji, X.; Guo, Z.; Wang, H. Plasma-induced amorphous shell and deep cation-site S doping endow $TiO_2$ with extraordinary sodium storage performance. *Adv. Mater.* **2018**, *30*, 1801013.

(19) Wang, B.; Zhao, F.; Du, G.; Porter, S.; Liu, Y.; Zhang, P.; Cheng, Z.; Liu, H. K.; Huang, Z. Boron-doped anatase $TiO_2$ as a high-performance anode material for sodium-ion batteries. *ACS Appl. Mater. Interfaces* **2016**, *8*, 16009−16015.

(20) Bai, Y. L.; Xarapatgvl, R.; Wu, X. Y.; Liu, X.; Liu, Y. S.; Wang, K. X.; Chen, J. S. Core-shell anatase anode materials for sodium-ion

batteries: the impact of oxygen vacancies and nitrogen-doped carbon coating. *Nanoscale* **2019**, *11*, 17860−17868.
(21) Koketsu, T.; Ma, J.; Morgan, B. J.; Body, M.; Legein, C.; Dachraoui, W.; Giannini, M.; Demortiere, A.; Salanne, M.; Mardoize, F.; Groult, H.; Borkiewicz, O. J.; Chapman, K. W.; Strasser, P.; Dambournet, D. Reversible magnesium and aluminium ions insertion in cation-deficient anatase $TiO_2$. *Nat. Mater.* **2017**, *16*, 1142−1148.
(22) Bi, H.; Zhu, S.; Liang, Y.; Jiang, H.; Li, Z.; Wu, S.; Wei, H.; Chang, C.; Cui, Z. Highly reversible electrochemical magnesium/lithium insertion performance in $TiO_2$(B) nanosheets with Ti cationic vacancies. *Chem. Eng. J.* **2022**, *442*, No. 136146.
(23) Guo, X.; Wang, C.; Wang, W.; Zhou, Q.; Xu, W.; Zhang, P.; Wei, S.; Cao, Y.; Zhu, K.; Liu, Z.; Yang, X.; Wang, Y.; Wu, X.; Song, L.; Chen, S.; Liu, X. Vacancy manipulating of molybdenum carbide MXenes to enhance Faraday reaction for high performance lithium-ion batteries. *Nano Res. Energy* **2022**, *1*, 9120026.
(24) Gao, P.; Chen, Z.; Gong, Y.; Zhang, R.; Liu, H.; Tang, P.; Chen, X.; Passerini, S.; Liu, J. The role of cation vacancies in electrode materials for enhanced electrochemical energy storage: synthesis, advanced characterization, and fundamentals. *Adv. Energy Mater.* **2020**, *10*, 1903780.
(25) Yang, J.; Huang, M.; Xu, L.; Xia, X.; Peng, C. Self-assembled titanium-deficient undoped anatase $TiO_2$ nanoflowers for ultralong-life and high-rate $Li^+/Na^+$ storage. *Chem. Eng. J.* **2022**, *445*, No. 136638.
(26) Yue, J.; Suchomski, C.; Voepel, P.; Ellinghaus, R.; Rohnke, M.; Leichtweiss, T.; Elm, M. T.; Smarsly, B. M. Mesoporous niobium-doped titanium dioxide films from the assembly of crystalline nanoparticles: study on the relationship between the band structure, conductivity and charge storage mechanism. *J. Mater. Chem. A* **2017**, *5*, 1978−1988.
(27) Yang, H.; Lan, C.-K.; Duh, J.-G. The power of Nb-substituted $TiO_2$ in Li-ion batteries: Morphology transformation induced by high concentration substitution. *J. Power Sources* **2015**, *288*, 401−408.
(28) Wang, S.; Pan, L.; Song, J. J.; Mi, W.; Zou, J. J.; Wang, L.; Zhang, X. Titanium-defected undoped anatase $TiO_2$ with p-type conductivity, room-temperature ferromagnetism, and remarkable photocatalytic performance. *J. Am. Chem. Soc.* **2015**, *137*, 2975−2983.
(29) Mizrahi, O.; Amir, N.; Pollak, E.; Chusid, O.; Marks, V.; Gottlieb, H.; Larush, L.; Zinigrad, D.; Aurbach, D. Electrolyte solutions with a wide electrochemical window for rechargeable magnesium batteries. *J. Electrochem. Soc.* **2008**, *155*, A103−A109.
(30) Liu, Y.; Pan, X.; Chen, W.; Zhao, X. Titanate-derived Nb-doped $TiO_2$ nanoparticles displaying improved lithium storage performance. *Dalton Trans.* **2022**, *51*, 2506−2511.
(31) Luo, L.; Zhou, K.; Lian, R.; Lu, Y.; Zhen, Y.; Wang, J.; Mathur, S.; Hong, Z. Cation-deficient $TiO_2$(B) nanowires with protons charge compensation for regulating reversible magnesium storage. *Nano Energy* **2020**, *72*, No. 104716.
(32) Xu, W.; Russo, P. A.; Schultz, T.; Koch, N.; Pinna, N. Niobium-doped titanium dioxide with high dopant contents for enhanced lithium-ion storage. *ChemElectroChem* **2020**, *7*, 4016−4023.
(33) Ma, J.; Li, W.; Morgan, B. J.; Świątowska, J.; Baddour-Hadjean, R.; Body, M.; Legein, C.; Borkiewicz, O. J.; Leclerc, S.; Groult, H.; Lantelme, F.; Laberty-Robert, C.; Dambournet, D. Lithium intercalation in anatase titanium vacancies and the role of local anionic environment. *Chem. Mater.* **2018**, *30*, 3078−3089.
(34) Chen, B.; Meng, Y.; Xie, F.; He, F.; He, C.; Davey, K.; Zhao, N.; Qiao, S. Z. 1D sub-nanotubes with anatase/bronze $TiO_2$ nanocrystal wall for high-rate and long-life sodium-ion batteries. *Adv. Mater.* **2018**, *30*, 1804116.
(35) Zhao, B.; Liu, Q.; Chen, Y.; Liu, Q.; Yu, Q.; Wu, H. B. Interface-induced pseudocapacitance in nonporous heterogeneous particles for high volumetric sodium storage. *Adv. Funct. Mater.* **2020**, *30*, 2002019.
(36) Yan, D.; Yu, C.; Li, D.; Zhang, X.; Li, J.; Lu, T.; Pan, L. Improved sodium-ion storage performance of $TiO_2$ nanotubes by $Ni^{2+}$ doping. *J. Mater. Chem. A* **2016**, *4*, 11077−11085.
(37) Alvar, E. N.; Zhou, B.; Eichhorn, S. H. Carbon-embedded mesoporous Nb-doped $TiO_2$ nanofibers as catalyst support for the oxygen reduction reaction in PEM fuel cells. *J. Mater. Chem. A* **2016**, *4*, 6540−6552.
(38) Li, W.; Bak, T.; Atanacio, A.; Nowotny, J. Photocatalytic properties of $TiO_2$ : Effect of niobium and oxygen activity on partial water oxidation. *Appl. Catal., B* **2016**, *198*, 243−253.
(39) Pan, L.; Wang, S.; Xie, J.; Wang, L.; Zhang, X.; Zou, J.-J. Constructing $TiO_2$ p-n homojunction for photoelectrochemical and photocatalytic hydrogen generation. *Nano Energy* **2016**, *28*, 296−303.
(40) Wang, Y.; Xue, X.; Liu, P.; Wang, C.; Yi, X.; Hu, Y.; Ma, L.; Zhu, G.; Chen, R.; Chen, T.; Ma, J.; Liu, J.; Jin, Z. Atomic substitution enabled synthesis of vacancy-rich two-dimensional black $TiO_{2-x}$ nanoflakes for high-performance rechargeable magnesium batteries. *ACS Nano* **2018**, *12*, 12492−12502.
(41) Saha, P.; Jampani, P. H.; Datta, M. K.; Hong, D.; Gattu, B.; Patel, P.; Kadakia, K. S.; Manivannan, A.; Kumta, P. N. A rapid solid-state synthesis of electrochemically active Chevrel phases ($Mo_6T_8$; T = S, Se) for rechargeable magnesium batteries. *Nano Res.* **2017**, *10*, 4415−4435.
(42) Zhao, W.; Zhang, Y.; Li, H.; Wang, K.; Jiang, K. Large-scale fabricating carbon coating Chevrel phase in molten salts: Implications for high-performance magnesium-ion battery cathode. *J. Alloys Compd.* **2022**, *925*, No. 166745.
(43) Li, Y.; Xu, D.; Zhang, D.; Wei, Y.; Zhang, R.; Guo, Y. Study on $MnO_2$/MXene-$Ti_3C_2$ composite materials as cathode materials for magnesium batteries. *RSC Adv.* **2019**, *9*, 33572−33577.
(44) Pei, C.; Yin, Y.; Liao, X.; Xiong, F.; An, Q.; Jin, M.; Zhao, Y.; Mai, L. Structural properties and electrochemical performance of different polymorphs of $Nb_2O_5$ in magnesium-based batteries. *J. Energy Chem.* **2021**, *58*, 586−592.
(45) Shan, P.; Gu, Y.; Yang, L.; Liu, T.; Zheng, J.; Pan, F. Olivine $FePO_4$ cathode material for rechargeable Mg-ion batteries. *Inorg. Chem.* **2017**, *56*, 13411−13416.
(46) Wu, D.; Zeng, J.; Hua, H.; Wu, J.; Yang, Y.; Zhao, J. $NaV_6O_{15}$: A promising cathode material for insertion/extraction of $Mg^{2+}$ with excellent cycling performance. *Nano Res.* **2020**, *13*, 335−343.
(47) Wu, D.; Zhuang, Y.; Wang, F.; Yang, Y.; Zeng, J.; Zhao, J. High-rate performance magnesium batteries achieved by direct growth of honeycomb-like $V_2O_5$ electrodes with rich oxygen vacancies. *Nano Res.* **2021**, 1−8.
(48) Ling, L.; Bai, Y.; Li, Y.; Ni, Q.; Wang, Z.; Wu, F.; Wu, C. Quick activation of nanoporous anatase $TiO_2$ as high-rate and durable anode materials for sodium-ion batteries. *ACS Appl. Mater. Interfaces* **2017**, *9*, 39432−39440.
(49) Di, A.; Wang, Y.; Zeng, H. C. $TiO_2$/C tetragons with a double-side concave nanostructure and its high rate performance on Na-ion storage. *Appl. Surf. Sci.* **2021**, *567*, No. 150756.
(50) Wang, N.; Gao, Y.; Wang, Y. X.; Liu, K.; Lai, W.; Hu, Y.; Zhao, Y.; Chou, S. L.; Jiang, L. Nanoengineering to achieve high sodium storage: A case study of carbon coated hierarchical nanoporous $TiO_2$ microfibers. *Adv. Sci.* **2016**, *3*, 1600013.
(51) Liu, H.; Cao, K.; Xu, X.; Jiao, L.; Wang, Y.; Yuan, H. Ultrasmall $TiO_2$ nanoparticles in situ growth on graphene hybrid as superior anode material for sodium/lithium ion batteries. *ACS Appl. Mater. Interfaces* **2015**, *7*, 11239−11245.
(52) Liu, X.; Zhu, S.; Liang, Y.; Li, Z.; Wu, S.; Luo, S.; Chang, C.; Cui, Z. 3D N-doped mesoporous carbon/$SnO_2$ with polypyrrole coating layer as high-performance anode material for Li-ion batteries. *J. Alloys Compd.* **2022**, *892*, No. 162083.


https://doi.org/10.1021/acsomega.2c07689
*ACS Omega* 2023, 8, 5893−5900